

Analysis and Interpretation of Frequency–Wavenumber Spectra of Young Wind Waves

FABIEN LECKLER

Service Hydrographique et Oceanographique de la Marine, Brest, France

FABRICE ARDHUIN AND CHARLES PEUREUX

Ifremer, Laboratoire d’Océanographie Spatiale, Centre de Brest, and Laboratoire de Physique des Océans, UMR 6523 CNRS-IFREMER-IRD-UBO, Plouzané, France

ALVISE BENETAZZO

Institute of Marine Sciences, National Research Council (CNR-ISMAR), Venice, Italy

FILIPPO BERGAMASCO

Università Ca’ Foscari di Venezia, Venice, Italy

VLADIMIR DULOV

Marine Hydrophysical Institute, Sebastopol, Russia

(Manuscript received 2 December 2014, in final form 7 June 2015)

ABSTRACT

The energy level and its directional distribution are key observations for understanding the energy balance in the wind-wave spectrum between wind-wave generation, nonlinear interactions, and dissipation. Here, properties of gravity waves are investigated from a fixed platform in the Black Sea, equipped with a stereo video system that resolves waves with frequency f up to 1.4 Hz and wavelengths from 0.6 to 11 m. One representative record is analyzed, corresponding to young wind waves with a peak frequency $f_p = 0.33$ Hz and a wind speed of 13 m s^{-1} . These measurements allow for a separation of the linear waves from the bound second-order harmonics. These harmonics are negligible for frequencies f up to 3 times f_p but account for most of the energy at higher frequencies. The full spectrum is well described by a combination of linear components and the second-order spectrum. In the range $2f_p$ to $4f_p$, the full frequency spectrum decays like f^{-5} , which means a steeper decay of the linear spectrum. The directional spectrum exhibits a very pronounced bimodal distribution, with two peaks on either side of the wind direction, separated by 150° at $4f_p$. This large separation is associated with a significant amount of energy traveling in opposite directions and thus sources of underwater acoustic and seismic noise. The magnitude of these sources can be quantified by the overlap integral $I(f)$, which is found to increase sharply from less than 0.01 at $f = 2f_p$ to 0.11 at $f = 4f_p$, and possibly up to 0.2 at $f = 5f_p$, close to the 0.5π value proposed in previous studies.

1. Introduction

Since the 1960s, the wave spectrum has been the most common way to characterize the sea state, with a wide

range of applications for, among others, marine meteorology, air–sea fluxes, remote sensing, and underwater acoustics. For a single-valued surface elevation $\zeta(x, y, t)$, the complete spectrum of the surface elevation is the three-dimensional (3D) spectrum $E(k_x, k_y, f)$. This full spectrum is only accessible to mapping instruments with high acquisition rates, such as systems based on video using stereo reconstruction from visible (Benetazzo 2006), infrared imagery (Sutherland and Melville 2013), or direct slope measurements from polarimetry (Zappa

 Denotes Open Access content.

Corresponding author address: Fabrice Ardhuin, Ifremer, ZI de la Pointe du Diable, CS 10070, 29280 Plouzané, France.
E-mail: arduin@ifremer.fr

DOI: 10.1175/JPO-D-14-0237.1

et al. 2012). Because such devices are still far from common, there are very few reports on the shape of the 3D spectrum. The signature of waves in light reflections (Dugan et al. 2001a) and radar backscatter at grazing angles (e.g., Plant and Farquharson 2012) suggests that the wave motion is nearly linear. Linearity combined with spatial homogeneity collapses the spectrum to a two-dimensional (2D) surface along the linear dispersion relation.

Snapshots of the sea surface have revealed important properties of the dominant and shorter waves, in particular the shape of the 2D spectrum from the pioneering work of Schumacher (1939) and Chase et al. (1957) to more recent efforts (Holthuijsen 1983; Banner et al. 1989; Hwang et al. 2000; Romero and Melville 2010; Yurovskaya et al. 2013). Still, nonlinear effects are expected to dominate the frequency spectrum of short gravity waves (Creamer et al. 1989; Janssen 2009; Krogstad and Trulsen 2010; Taklo et al. 2015), making difficult the investigation of the energy balance between wind-wave generation, dissipation, and nonlinear wave-wave interactions that are expected to determine the shape of the wave spectrum. There is also a need to resolve wave directions without the 180° ambiguity of 2D snapshots used by, for example, Banner et al. (1989) and Yurovskaya et al. (2013), in particular for the interpretation of radar Doppler signal or underwater acoustics (Farrell and Munk 2008; Duennebieer et al. 2012).

Here, we take advantage of recent improvements in stereo video processing (Gallego et al. 2008; Fedele et al. 2013; Benetazzo et al. 2014) to investigate the properties of short gravity waves. It is possible to resolve very short waves by using the image radiance, with methods developed by Gallego et al. (2011) and Yurovskaya et al. (2013), or light polarization as demonstrated by Zappa et al. (2012), but these methods require complex processing or equipment that was not available to us. Here, we only use the geometry derived from the correlation of stereo pairs, which allows us to resolve waves with wavelengths between 0.6 and 11 m, and young wave ages. This is the first analysis of in situ data in which the free waves and their bound harmonics can be separated. The data acquisition and processing are described in section 2. Our analysis covers the spectral shapes in section 3, with particular attention on nonlinear effects in section 4, and the directional spectrum and its consequences for the generation of seismic and acoustic waves in section 5. Conclusions follow in section 6.

2. Data acquisition and processing

The experiment was conducted in September and October 2011 from the research platform of the Marine Hydrophysical Institute. The platform is located 500 m

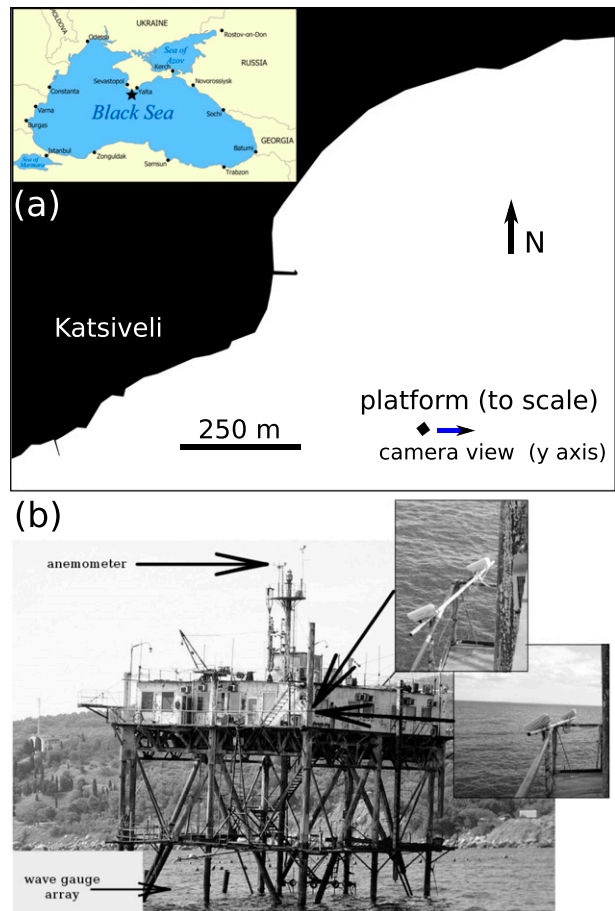


FIG. 1. (a) Location of the Katsiveli platform and (b) pictures of the platform looking toward the northeast. Inset shows two views of the same camera installation, seen from above and from the northwest.

off the coast next to Katsiveli in the Black Sea, near the southern tip of Crimea. The water depth at the observation area is about 30 m. As shown in Fig. 1, the platform is exposed to deep-water waves coming from directions 90° to 250° .

The wind speed and direction are measured at the center of the platform, 23 m above mean sea level. Wind and wave measurement locations are shown in Fig. 1. The sea surface elevation is measured at a 10-Hz sampling frequency and 2-mm accuracy with an array of six wave gauges. Finally, the Wave Acquisition Stereo System (WASS) acquires image sequences of the sea surface and is mounted 12.25 m above the sea surface. This is a different system from the stereophotographic system developed by Kosnik and Dulov (2011) and analyzed in Yurovskaya et al. (2013). That other system was mounted on the same platform, although at a lower elevation. Compared to that other system, we are investigating longer waves with a large field of view, and we use the time evolution of the free

surface. Our WASS consists of a pair of synchronized 5-megapixel (2048×2456 pixels) BM-500GE JAI cameras, each equipped with a 5-mm focal length low distortion lens to ensure a large common field of view. The intrinsic parameters (i.e., focal length, principal point, and distortion parameters) of each camera were calibrated using the camera calibration toolbox by Jean-Yves Bouguet. The relative position between the two cameras (i.e., the extrinsic parameters) was computed by first recovering the essential matrix with the autocalibration algorithm of [Hartley and Zisserman \(2003\)](#) and then setting the scale using a known calibration target. Full details of camera calibration procedure can be found in [Leckler \(2013\)](#).

The data described here were acquired on 4 October 2011, with a well-established wind direction from west-southwest and a growing speed, from less than 2 m s^{-1} before 1100 local time (LT) up to 14 m s^{-1} by 1400 LT. [Figure 2](#) shows the wind and wave conditions during the video acquisitions. We note that the sea state corresponds to a very young wind sea with wave age C_p/U_{23} from 0.35 to 0.42. Here, we focus on record number 3, starting at 1307 LT, on 4 October 2011. Records 2 and 4 show similar results with a slightly less or more developed wind sea. Over the entire record, the significant wave height is $H_s = 0.45 \text{ m}$, with a peak frequency of 0.33 Hz , and the mean wind speed is 13.2 m s^{-1} .

The processing of the video data is described in detail by [Leckler \(2013\)](#) and builds on the work of [Benetazzo \(2006\)](#). The general principle is as follows: starting from the left image, each pixel is associated with a pixel in the right image. This association is based on a maximum correlation between two windows of the image surrounding the pixels to be matched. Two main sources of error may hinder the accuracy of stereo reconstruction when applied to the sea surface. First, specular sun reflections can give high correlation (one bright spot correlates well with any other bright spot) without corresponding to the same point of the sea surface because the two cameras have different view angles and thus do not see the same specular points. This effect was taken into account when choosing both the position of the cameras and the time of acquisition as a function of the sun position. Second, whitecaps, even if they correspond to the same point in the two cameras, introduce such a strong inhomogeneity in the brightness that they bias the window-based matching process. To mitigate that effect, [Leckler \(2013\)](#) introduced a histogram equalization combined with a pyramidal search algorithm in three steps, starting from large windows and refining to smaller windows. This procedure reduced considerably the error in matching of points around whitecaps.

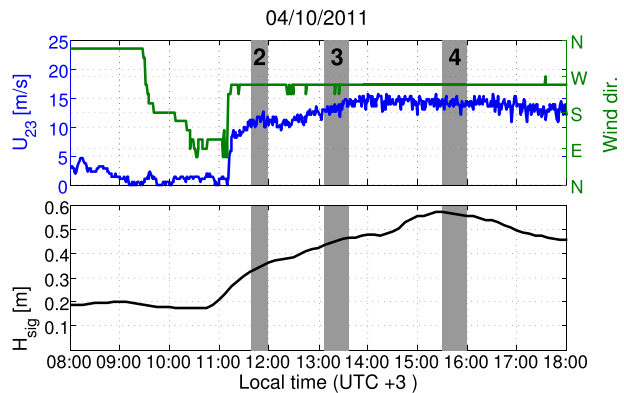


FIG. 2. Time series of wind speed and direction obtained from the anemometer at 23 m height above the mean sea level, and time series of significant wave height from the wave gauge array. The gray shaded areas numbers 2, 3, and 4 correspond to the time frame of the stereo video records of the 2011 experiment that are analyzed in [Leckler \(2013\)](#).

For each pair of matching points, the geometry of view gives the position (x, y, z) of the sea surface elevation in world coordinates. Hence, the set of all pairs of points yields a cloud of points on the sea surface. This cloud is then gridded with a linear interpolation at a resolution of 5 cm in each direction to produce a discretized surface elevation map $\zeta(x, y, t)$. Because of the strong heterogeneity of the density of the point cloud, which is denser closer to the cameras, the average distance of matched points tends to 10 cm for the furthest part of the reconstruction. Hence, the 5 cm are an oversampling for only part of the image.

Our processing is thus sequential; each of the 21 600 image pairs acquired at 12 frames per second is treated independently from the others. The end result is a 30-min evolution of the wavy sea surface with an area of about $15 \times 20 \text{ m}^2$.

Here, the x axis is along the cameras' supporting bar; the y axis points away from the cameras, and the z axis is up. Examples of the stereo pair and reconstructed free-surface geometry can be seen in [Fig. 3](#) for frames number 8 and 12 of the record analyzed here. The chosen video frames reveal a wide variety of directions for short waves. This variety will be investigated using spectral analysis. For this, we selected a reduced area, 10.8 by 10.8 m^2 , based on criteria of complete data coverage and homogeneity of the mean square slopes along the x and y axis. Using the method of [Benetazzo et al. \(2012\)](#), we find that the expected accuracy of the stereo triangulation for the elevation is 1 cm with 95% confidence.

3. Spectra and dispersion relations

The spectrum $E(k_x, k_y, f)$ is obtained after applying a Hamming window in all three dimensions to the

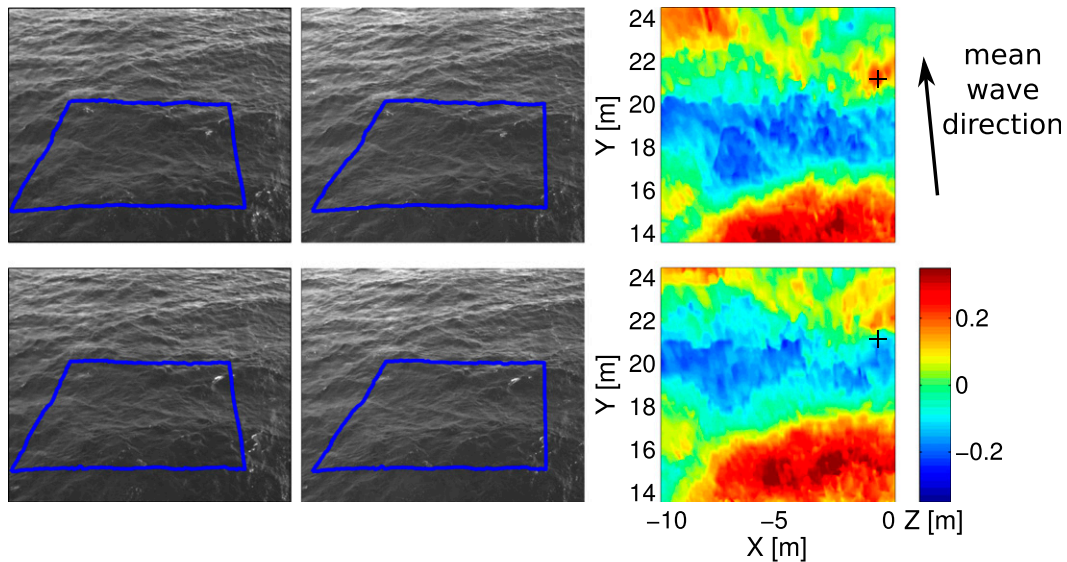


FIG. 3. Example of two pairs of images and the corresponding stereo reconstructed surface, separated by 0.33 s (four frames): (top) the first and (bottom) the last. Images have been corrected for lens distortion. Blue contours represent the footprints of the reconstructed surface on images. The black cross in the elevation map is at the same ($x = -0.5$, $y = 21.2$) location.

elevation maps $\zeta(x, y, t)$ over time intervals of 85.25 s (1024 frames) and averaging the modulus squared of the three-dimensional Fourier transform over 39 overlapping time intervals, that is, 20 independent intervals giving 40 degrees of freedom for each spectral density in (k_x, k_y, f) space. Different time-window lengths and the use of detrending in time and/or space had little impact on the results shown here. Figure 4 shows that this processing is consistent in terms of spectral level with data from wave gauges up to 1.4 Hz, with a strong overestimation at higher frequencies. Given that the raw data have a Nyquist frequency at 6 Hz, we tried to extend the useful frequency range beyond 1.4 Hz by smoothing the data in space and time. This attempt was not very successful as a 3 pixel by 3 pixel smoothing kernel combined with a 5-point Hann window already reduced the energy by 20% at 1 Hz and by a factor of 2 at 1.4 Hz. We thus preferred to work with the raw data. Since we particularly wish to investigate waves as short as possible, we will work with the spectra obtained from the raw data, which are consistent with the wave gauge spectrum up to 1.4 Hz.

We have tested the data for stationarity by looking at possible evolutions of the spectral density between the first and last 10 min. There is a weak downshift of the peak frequency from 0.33 to 0.30 Hz, accompanied by an increase in wave height from 0.42 to 0.52 m. Still, the spectral distributions shown in Figs. 5 and 6 are qualitatively similar to the ones obtained over 10 min only.

Here we prefer to show the spectrum over 30 min as it is less noisy, with a 50% error (2 dB) at the full spectral resolution and 95% confidence interval.

The Fourier transform converts the physical space (x, y, t) into a 3D space (k_x, k_y, f) . We will first characterize the wave spectrum using slices in this 3D space, and later we will integrate along one dimension to recover the more usual 2D spectra. Such 3D spectra were already shown by Dugan et al. (2001b,a), but they were spectra of light intensity and not surface elevation. Only recently measurements of the 3D spectrum of elevation have been produced by Gallego et al. (2008) and Fedele et al. (2011, 2013), using the same stereo video system, with an emphasis on the dominant wave properties and space–time extremes (Fedele 2012). Here, we will focus on short waves at frequencies 3 to 5 times above the peak frequency.

As expected, the wave energy is mostly located around the linear dispersion relation for a uniform current

$$2\pi f = \sqrt{gk \tanh(kD)} + kU \cos(\theta - \theta_U), \quad (1)$$

where D is the water depth, g is the acceleration of gravity, U is the current magnitude, θ is the wave direction, and θ_U is the current direction. In theory, U and θ_U are themselves functions of k and θ because of the vertical shear of the current (Andrews and McIntyre 1978; Kirby and Chen 1989), and the nonlinear correction to the phase speed that can be interpreted as the

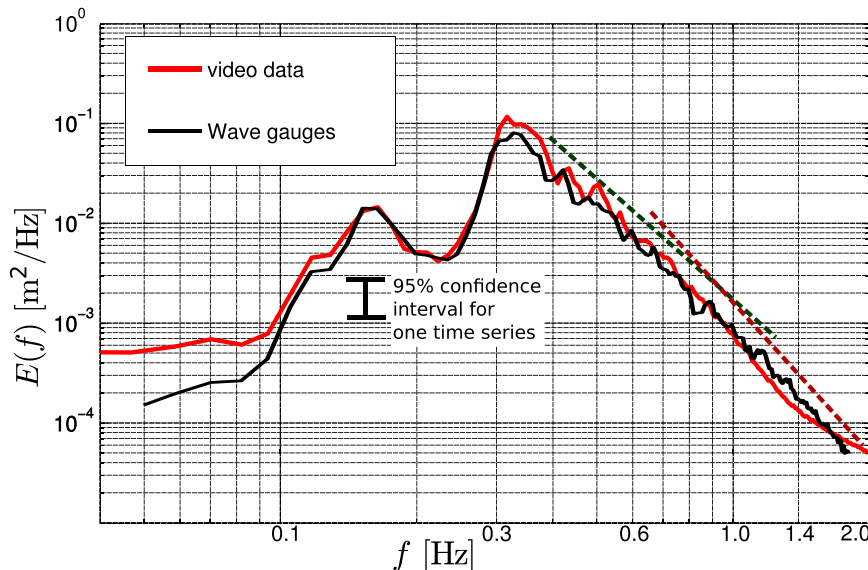


FIG. 4. Frequency spectrum $E(f)$ estimated from the stereo video system, without any smoothing, and from the wire wave gauges mounted on the platform. The dashed lines show the f^{-4} and f^{-5} asymptotes. The error bar corresponds to random sampling errors for single time series, as given by the expected χ^2 distribution with 40 degrees of freedom. The spectrum from the video is averaged over the 10.8-m square analysis window, and thus the random sampling error is actually smaller for the shorter waves with many uncorrelated waves in the field of view.

advection of waves by the Stokes drift (Andrews and McIntyre 1978; Stewart and Joy 1974; Broche et al. 1983; Ardhuin et al. 2009). Here, we did not attempt to estimate these variations of U , and we find a general good agreement by taking a constant $U = 0.15 \text{ m s}^{-1}$ and $\theta_U = 279^\circ$. This current velocity contains effects of large-scale flows and wind-driven currents. Because of the current orientation, 10° off our y axis, the shift of the dispersion relation caused by the current is clearly visible on the f - k_y slice through the spectrum, shown in Fig. 5b, with an asymmetry between waves propagating toward the positive y and negative y directions. Such an asymmetry is not visible at frequencies below 1.5 Hz in the f - k_x slice shown in Fig. 5c.

In a previous investigation on the short-wave spectrum, Banner et al. (1989) discussed the “kinematic Doppler dispersion” showing that it could contribute to a deviation of the frequency spectrum from f^{-5} in the case of young waves. The relative change in wavenumber for an oscillatory current is equal to the long-wave slope, here $ka_{\text{rms}} = 0.07$, where a_{rms} is the root-mean-square surface elevation amplitude, while the apparent frequency is unchanged (e.g., Garrett and Smith 1976). Consistent with the results shown in Banner (1990) for $ka_{\text{rms}} = 0.1$ and $ff_p < 5$, this Doppler effect is not enough to cause a significant modification of the dispersion relation. For our case, it gives a $\pm 7\%$ expected modulation of the wavenumber for short waves in the

direction of the dominant waves, which is consistent with the thickness of the energy distribution around the theoretical dispersion relation, as shown in Fig. 6. More interestingly, the slices at $f = 1 \text{ Hz}$ and higher frequencies reveal a significant contribution inside of the dotted white line, from waves longer than predicted by the linear dispersion relation. In particular, Fig. 6f exhibits a crescent-shaped distribution that is the same as the shape in Fig. 6a but at twice the wavenumber and twice the frequency. These components (f, k_x, k_y) in Fig. 6f are thus likely dominated by the nonlinear harmonics of the $(f/2, k_x/2, k_y/2)$ components in Fig. 6a. Records 2 and 4 show analogous patterns (see Figs. 3.22–3.24 in Leckler 2013).

4. Nonlinear effects

In this section, we will verify that the magnitude of the observed energy away from the linear dispersion relation can be predicted from weakly nonlinear theory. Nonlinear effects are well known, starting from the sharper crests of waves pointed out by Stokes (1880), which is usually interpreted as the presence of harmonic waves, that is, Fourier components with wavenumbers and frequencies k and f such that $[2\pi f - kU \cos(\theta - \theta_U)]^2 > gk \tanh(kD)$. A second-order approximation of this effect is used, for example, in the analysis of wave height distributions to explain the crest heights of

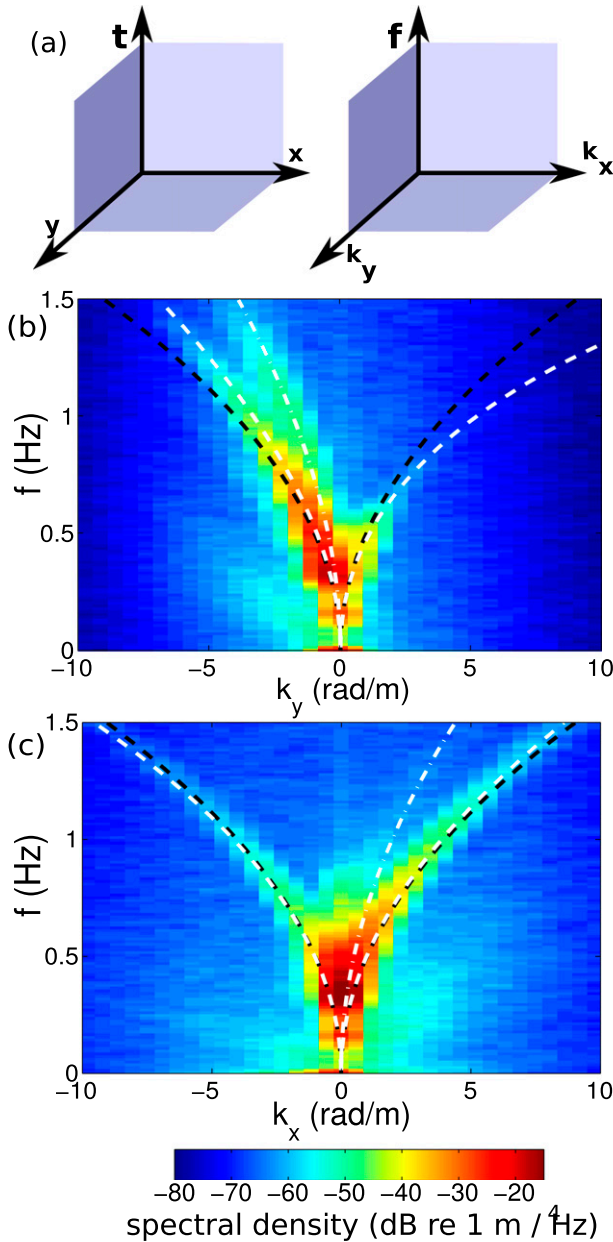


FIG. 5. (a) Schematic of the three-dimensional data cube and spectrum cube. The (b) f - k_y , and (c) f - k_x slices of the double-sided 3D spectrum. The black dashed line marks the linear dispersion relation without the current, and the white dashed line marks the linear dispersion relation with a uniform current $U = 0.15 \text{ m s}^{-1}$ from the trigonometric angle 279° . The white dashed-dotted line marks the dispersion relation for first harmonic, with the same current.

extremely large waves (e.g., Tayfun 1980). In the case of spectra for a random sea, Hasselmann (1962) showed how the wave power spectrum can be expanded in a power series of the wave steepness. In this expansion, the first term is of second order, it is the contribution E_{lin} given by the linear waves. The next term is the fourth-order

contribution E_4 . The term E_4 contains the power spectrum of the second-order waves $E_{2,2}$ given by Weber and Barrick (1977), that is, the same contribution that gives crests sharper than troughs. The term E_4 contains another contribution, the “quasi-linear” term $E_{3,1}$ that is due to the correlation of third-order and first-order waves. Given the convex dispersion relation of surface gravity waves, all spectral components contributing to $E_{2,2}$ have wavenumber vectors $\mathbf{k} = \mathbf{k}_1 \pm \mathbf{k}_2$ and frequencies $f = f_1 \pm f_2$ that do not correspond to the linear dispersion given by Eq. (1). Hence, it is possible to identify in our data the $E_{2,2}$ contribution. On the contrary the $E_{3,1}$ terms share the same dispersion relation and are not readily isolated in measurements. However, these contributions to the spectrum at wavenumber vectors \mathbf{k} and f are such that $\mathbf{k}_1 + \mathbf{k}_2 = \mathbf{k}_3 + \mathbf{k}$ and $f_1 + f_2 = f_3 + f$. These two conditions define the “resonant manifold” for the four-wave interactions.

Our purpose here is to interpret the observed wave spectrum as this sum of E_{lin} and E_4 by isolating the E_{lin} components. We propose that most of the energy on the resonant manifold belongs to E_{lin} . This proposition is verified qualitatively by computing the expected value of E_4 caused by the nonresonant interactions at both the second and third order. From the Zakharov equation, the canonical transformation of Krasitskii (1994) assuming Gaussian statistics, Janssen [2009, see Eqs. (31)–(35) therein] derived an equation that expresses E_4 as a function of E_{lin} , including both $E_{2,2}$ and $E_{3,1}$. This is what we have applied here.

This computation of E_4 requires a well-resolved directional spectrum for the dominant waves. For frequencies above 0.5 Hz, we have first transformed the spectral coordinates to use the intrinsic frequency $\sigma/(2\pi)$ instead of the apparent frequency $\omega/(2\pi)$. The linear part E_{lin} was estimated by taking all the energy outside of the white dotted lines in Fig. 6, corresponding to $k > 0.83\sigma^2/g$. This gives a high-frequency part of the spectrum.

For frequencies below 0.5 Hz, we have estimated elevations and slopes in the x and y direction at the center of the analysis region, using a finite difference over 50 cm for frequencies less than 0.5 Hz. From this heave, pitch, and roll series, we have applied standard buoy processing techniques (Longuet-Higgins et al. 1963) and the maximum entropy method (MEM) of Lygre and Krogstad (1986) to obtain the frequency–direction spectrum $E(f, \theta)$. This low-frequency spectrum is joined with the high-frequency spectrum at 0.5 Hz, with a moderate discontinuity.

The resulting frequency–direction spectra are compared in Fig. 7. First of all, it is interesting to note that the largest differences between the full spectrum

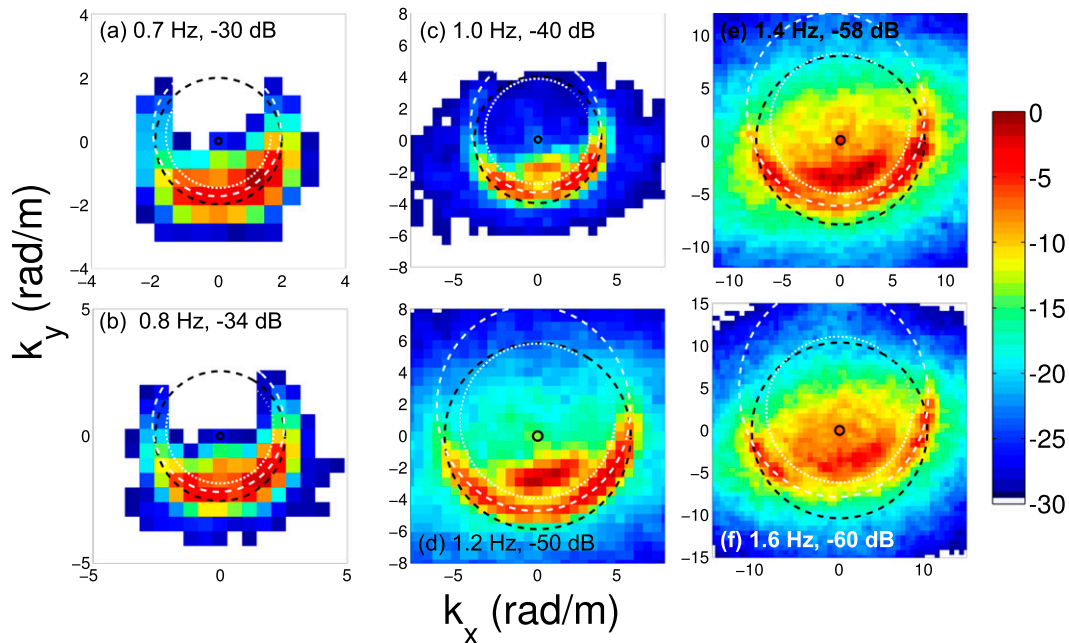


FIG. 6. Slices of the double-sided spectrum for positive apparent frequencies 0.7, 0.8, 1.0, 1.2, 1.4, and 1.6 Hz. The energy appears in the direction from where it is coming. For each panel, the color scale spans 30 dB with the dark red corresponding to the power indicated in the figure (e.g., -30 dB) relative to $1 \text{ m}^4 \text{ Hz}^{-1}$. Note that 1.4 and 1.6 Hz are twice 0.7 and 0.8 Hz, so that the first harmonic of the components in (a) and (b) appear at approximately twice the wavenumbers in (e) and (f). In each panel, the linear dispersion relation without current is plotted in black, and the white dashed line gives the linear dispersion with a uniform current $U = 0.15 \text{ m s}^{-1}$ oriented toward the trigonometric angle 99° . The white dotted line marks approximately the separation between the linear part of the spectrum and the faster nonlinear components.

(Fig. 7a) and the linear part (Fig. 7b) first appear in the wind direction (about 280° relative to the x axis) at frequencies above $3f_p$. These differences increase toward higher frequencies with a clear gap between the two maxima on either side of the wind direction in the linear part of the spectrum. This gap is almost absent in the full spectrum because it is hidden by the nonlinear part $E_{2,2}$ of the spectrum E_4 . Finally, the theoretical nonlinear correction of Fig. 7b is shown in Fig. 7c and the correction brings it closer to the full spectrum in Fig. 7a.

When integrated over the directions, the measured spectral densities can be compared to earlier measurements. The nondimensional spectral density $f^5 E(f)/g^2$ is usually called the “saturation spectrum.” We find that the full normalized single-sided spectrum is fairly stable at $f^5 E(f)/g^2 \simeq 8 \times 10^{-6}$ from $2f_p$ to $4.25f_p$ (Fig. 8), which means that the linear part of the normalized spectrum actually decreases faster than f^{-5} toward high frequencies. The value of the saturation $f^5 E(f)/g^2$ corresponds to the Joint North Sea Wave Project (JONSWAP) data (Hasselmann et al. 1973), but it is 30% lower than the data analyzed by Forristall (1981). Looking at the wavenumber spectrum, we have a corresponding saturation level $k^3 E(k) \simeq 0.010$, a value that is comparable to the

0.008 determined for more developed waves by Romero and Melville [2010, their Eq. (35)], which is very close to the 0.0078 given when converting Eq. (5.1) in Banner et al. (1989) from cycles per meter to radians per meter.

5. Discussion of directional properties

Using common conventions we define the spectral density $E(k, \theta)$ by taking twice the integral over negative frequencies so that the sum over all positive k and all angles from 0 to 2π give the surface elevation variance. Here, we use two complementary definitions for the downwind and crosswind spectra, as illustrated in Fig. 8.

In the first definition, we select waves propagating exactly in one direction modulo π , for example, the upwind or downwind direction with $\pi k^3 [E(k, 0) + E(k, \pi)]$. The addition of energy in opposite directions makes it comparable to measurements in which the direction of propagation is not available, such as the scanning contour radar data of Romero and Melville (2010). Such a saturation in the upwind or crosswind direction should be related to the intensity of radar echoes in these directions, with the addition of an upwind–downwind asymmetry that is associated with non-Gaussian effects

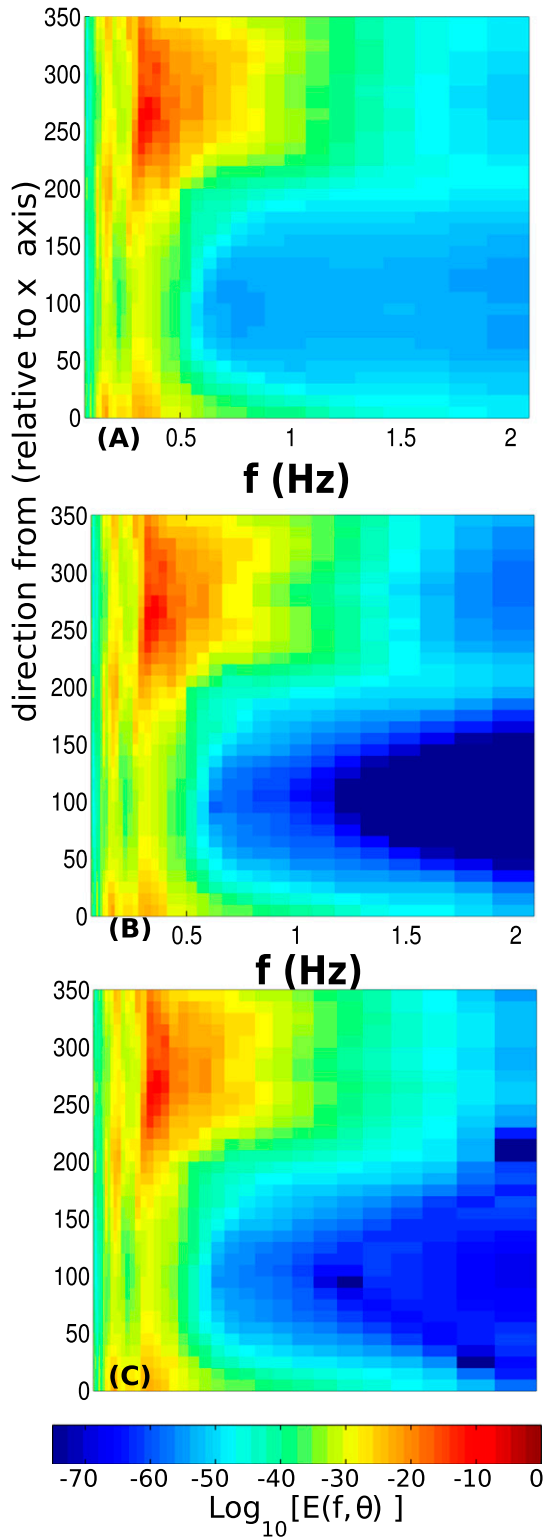


FIG. 7. Three estimates of frequency–direction spectrum $E(f, \theta)$ given by (a) integrating the 3D spectrum over all wavenumbers magnitudes, (b) only for components in the “linear part” of the spectrum, and (c) estimated from the nonlinear correction $E_{lin} + E_4$ to a “linear spectrum” E_{lin} . Here, the frequency is the intrinsic frequency $\sigma/(2\pi)$ and for each spectrum we have used the maximum entropy method of Lygre and Krogstad (1986) for $f < 0.45$ Hz.

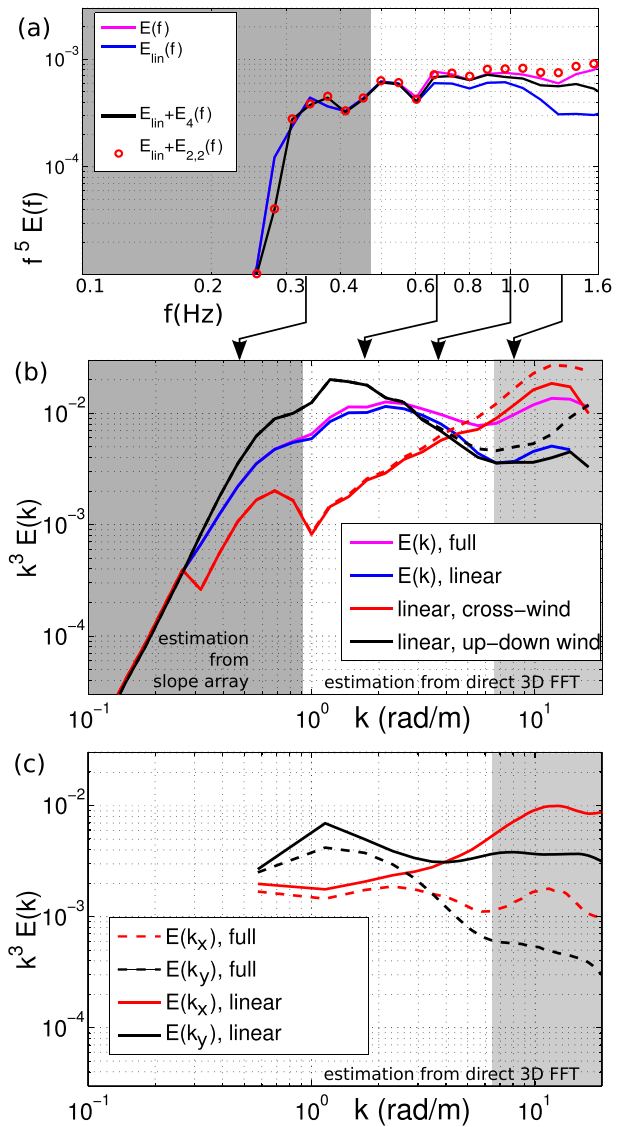


FIG. 8. (a) Estimates of the frequency spectrum multiplied by f^5 , using the intrinsic frequency. The linear part E_{lin} is obtained by integrating the energy only around the dispersion relation; $E_{lin} + E_{2,2}$ corresponds to the partial nonlinear correction following Weber and Barrick (1977), while the full nonlinear correction is $E_{lin} + E_4$ and matches fairly well the observed spectrum $E(f)$. (b) Saturation spectrum $k^3 E(k)$ estimated from the full spectrum or the linear part only, and saturation spectrum in two directions $\pi k^3 [E(k, \theta_0) + E(k, \theta_0 + \pi)]$ with $\theta_0 = 0$ in red (crosswind) and $\theta_0 = \pi/2$ in black (downwind and upwind). The multiplication by π collapses the curves for an isotropic spectrum. For these two directions, the solid lines come from the linear part of the spectrum, and the dashed line comes from the full spectrum. (c) Saturation in the x and y direction, similar to the $k_i^3 \phi(k_i)$ in Fig. 4 of Banner et al. (1989). The shaded region at low frequency corresponds to the part of the spectrum estimated using a slope array analysis. The shading at high frequency covers the range of wavenumbers for which directional parameters are likely to be strongly influenced by noise.

in the short-wave modulation (e.g., Quilfen et al. 1999). In our data, for $k > 9k_p$, slopes in the crosswind direction are steeper than in the upwind–downwind direction, and crosswind slopes grow to be as large as 3 times the upwind–downwind slopes at $16k_p$ that corresponds to $4f_p$. This predominance of crosswind slopes is more important than anticipated by Elfouhaily et al. (1997), but it is in line with the larger spectral densities in the crosswind directions also for $k > 9k_p$ in Romero and Melville (2010). This feature could explain part of the similarly dominant crosswind echoes in L-band scatterometer data found at low winds by Yueh et al. (2013).

The second definition follows Banner et al. (1989) and is illustrated in Fig. 8c, using wavenumbers in one dimension only, for example, for the x wavenumber:

$$E(k_x) = \int_{-\infty}^{\infty} \int_{-\infty}^{\infty} E(k_x, k_y, f) dk_y df, \quad (2)$$

which combines components with wavenumbers k and directions θ such that $k = k_x/\cos(\theta)$. Because of the sharp roll of the wavenumber spectrum $E(k_x, k_y)$ for large $k = \sqrt{k_x^2 + k_y^2}$, the spectral density $E(k_x)$ is generally dominated by values near the wavenumber vector $\mathbf{k} = (k_x, 0)$. Compared to the 1D spectra of Banner et al. (1989) and Banner (1990) that roll off regularly like k^{-3} between wavelengths of 1.5 m and 20 cm, our downwind and k_y spectra only roll off slightly faster than k^{-3} between 6 and 1 m. For wavelengths between 1 and 2 m, we have a roughly constant direction-integrated spectrum when multiplied by k^3 (magenta line in Fig. 8b) but a clear increase in the crosswind saturation (dashed red line) and a decrease in the downwind saturation (dashed black line). This transition from a larger downwind slope for long waves to a larger crosswind slope for short waves is less pronounced but still noticeable when using projections of the spectrum on the x and y axes, or Banner's 1D spectra, and it appears at $k \simeq 4 \text{ rad m}^{-1}$. A similar transition appears at a wavenumber $k \simeq 6 \text{ rad m}^{-1}$ in experiment 4 of Banner et al. (1989), with a similar wind speed of 13 m s^{-1} but a much more developed sea state. This difference supports the idea that the transition may vary with the wave age, occurring at higher wavenumbers for more mature waves. In the more mature conditions, the dominant waves may have less a modulation effect on the shorter components. Also, the wind-induced surface drift, which is expected to favor wave breaking (Banner and Phillips 1974), may be reduced by a stronger upper-ocean mixing (e.g., Raschle and Ardhuin 2009). More data will be needed to test these hypotheses, with different wave ages and covering a wide range of scales.

The dominant crosswind propagation is associated with a large and deep gap in the directional spectrum

between the two maxima, with a difference of direction growing from 100° at $3f_p$ to 150° at $4.25f_p$. This is better seen in Fig. 9a, which shows the full directional spectrum with a single broad peak and the spectrum of the linear waves with these two peaks with a clear gap in between. This difference is due to the nonlinear spectrum that is relatively well predicted by the canonical transformation (dashed line). When one includes only the term $E_{2,2}$, the spectral level is strongly overestimated (red circles). The quasi-linear term $E_{3,1}$ is necessary to conserve the energy as discussed by Janssen (2009). Such a bimodal directional spectrum was already measured by Long and Resio (2007), Hwang et al. (2000), Young (2010), and Romero and Melville (2010) in the 2D wave spectra and suggested from the interpretation of buoy measurements by Ewans (1998). These previous datasets gave a maximum angular distance of 120° , but they were limited to $k/k_p < 12$. Our data thus suggest that the directional distribution keeps broadening, at least up to $k/k_p \simeq 25$. This broadening is also clearly seen in Figs. 3.22–3.24 in Leckler (2013) for all records. We also confirmed these directional properties using wave gauge data. Directional distributions estimated with a direct method of triplet analysis (Krogstad 2005) showed the same angular broadening as for stereo-derived spectrum, up to $f = 1.4 \text{ Hz}$.

Because Ewans (1998) used directional spectra estimated from buoy displacements processed with the maximum entropy method of Lygre and Krogstad (1986), we have also included the MEM-estimated spectrum from the heave and slopes time series computed from our 3D surfaces. Figure 9b compares three directional spectra that have the same energy and different distributions. Namely, the full second-order spectrum E_4 when added to E_{lin} gives a good approximation of the full spectrum E . The usual estimate of the directional spectrum from heave and slope estimates gives a different distribution. Interestingly, this estimate is between the shape of the frequency spectrum and the shape of the wavenumber spectra shown in Fig. 9c. In Fig. 9c, the directional distribution $E_{\text{MEM}}(k, \theta)$ is estimated from $E_{\text{MEM}}(f, \theta)$ using the linear wave dispersion relation. Further, and only for this figure because we are trying to analyze the data at the limit of validity of the measurements, contributions to the full spectrum from apparent frequencies above 1.62 Hz have been discarded in order to minimize noise contamination from higher frequencies. This filtered spectrum is thus not too different from the linear part of the spectrum because the filtering removes both noise and harmonics.

This result could be related to the fact that slopes are related to the shape of the waves and hence the wavenumbers. We note that there are other possible alternatives to MEM (e.g., Benoit et al. 1997), which will likely produce

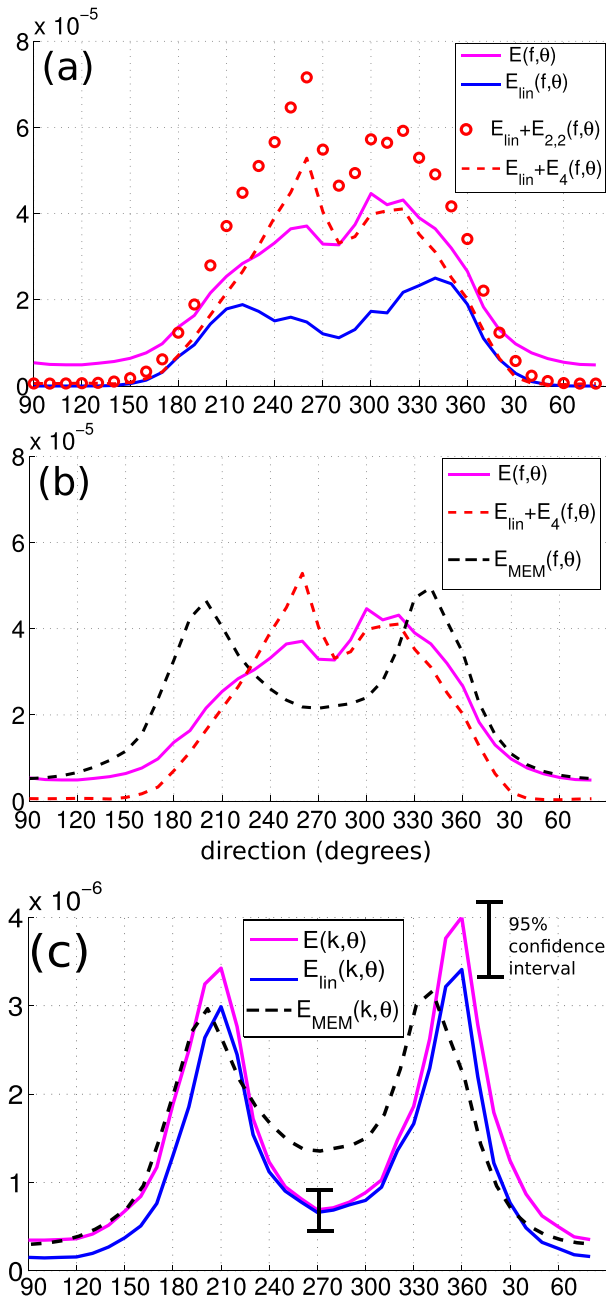


FIG. 9. (a) Linear E_{lin} and nonlinear $E_4 = E_{2,2} + E_{3,1}$ contributions to the directional wave spectrum at the intrinsic frequency $f = 1.42 \text{ Hz} = 4.25f_p$. (b) Compared directional distribution from the full spectrum, the one reconstructed from the linear part and $E_{MEM}(f, \theta)$ estimated from heave and slopes using the maximum entropy method. (c) Directional distributions for the wavenumber spectra, for the full spectrum, linear part and $E_{MEM}(k, \theta)$ estimated from $E_{MEM}(f, \theta)$ assuming linear wave dispersion. The error bar of $\pm 25\%$ corresponds to the error expected with 120 degrees of freedom, consistent with a directional resolution of 15° , 3 times coarser than the true resolution at $f = 1.42 \text{ Hz}$.

different results. However, MEM and all other methods based on heave and slope data at a single point tend to produce two peaks if the four directional moments given by the heave and slope cospectra are not consistent with a single peak. In the case of a waverider buoy, as used by [Ewans \(1998\)](#), the nonlinear components of the sea surface elevation are almost completely removed as the buoy follows the wave orbital motion. Hence, the bimodality reported by [Ewans \(1998\)](#) is more likely to be real, as confirmed by our experiment and others.

We will not discuss here all the possible generating mechanisms for these waves at very oblique angles relative to the wind, and we only mention here the possible generation of short waves by long breaking waves introduced by [Kudryavtsev et al. \(2005\)](#) to explain the roughness contrast in remote sensing data over current features. This mechanism was also mentioned by [Duennebieer et al. \(2012\)](#) to explain the strong variability at 1–10-Hz frequencies in acoustic data. In wavenumber, the effect of nonlinearity has little effect on the shape of the directional distribution, as shown in [Fig. 9b](#), as expected from [Janssen \(2009\)](#). This shows that usual remote sensing techniques, using wavenumber spectra, are easier to interpret than frequency–direction spectra, as long as the 180° ambiguity is not a problem. This ambiguity, however, must be removed in order to analyze acoustic or seismic data.

Indeed, we recall that when the seawater compressibility is taken into account, the second-order wave–wave interaction is also responsible for the generation of acoustic and seismic waves in the ocean and atmosphere ([Longuet-Higgins 1950](#)) with a radiated power that is proportional to the spectral density of the second-order pressure at near-zero wavenumber ([Hasselmann 1963](#)). For linear waves in deep water, this is given by

$$F_{p2,surf}(\mathbf{K} \simeq 0, f_s) = \rho_w^2 g^2 f E^2(f) I(f), \quad (3)$$

with the overlap integral defined by [Farrell and Munk \(2008\)](#) as

$$I(f) = 2 \int_0^\pi E(f, \theta) E(f, \theta + \pi) d\theta / \left[\int_0^{2\pi} E(f, \theta) d\theta \right]^2, \quad (4)$$

which for linear waves with k uniquely related to f is the same as

$$I(f) = 2 \int_0^\pi E(k, \theta) E(k, \theta + \pi) d\theta / \left[\int_0^{2\pi} E(k, \theta) d\theta \right]^2. \quad (5)$$

A correction for finite water depth is given in [Ardhuin and Herbers \(2013\)](#).

The integral $I(f)$ provides a possible key to the estimation of the wave spectrum $E(f)$ from acoustic

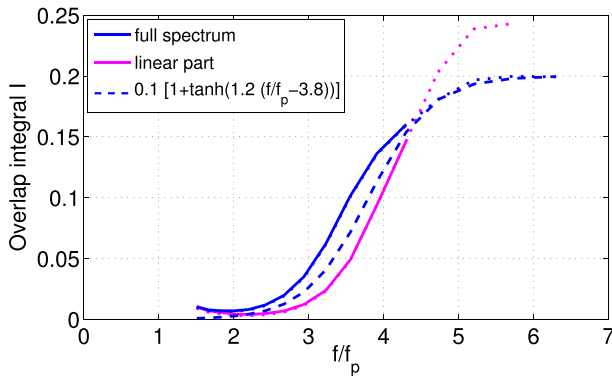


FIG. 10. Overlap integral as a function of intrinsic frequency normalized by the peak frequency. The integral was computed from the wavenumber–direction spectrum $E(k, \theta)$ such as shown in Fig. 9. The lines are dotted at high frequencies where noise is likely to be significant.

measurements. In particular, assuming that acoustic propagation is linear, the relative variations of acoustic power are proportional to $E^2(f)I(f)$. Observations show a clear variation of the acoustic power as a function of observed wind speed (Farrell and Munk 2010; Duennebier et al. 2012) or modeled wave spectral parameters (Ardhuin et al. 2013). In particular, the wave model of Ardhuin et al. (2013) clearly fails to predict the increase in acoustic power with wind speeds increasing above 7 m s^{-1} and at frequencies above 0.5 Hz. There is thus a need to better understand the variations of $I(f)$ to estimate $E(f)$ or vice versa.

Figure 10 shows the overlap integral $I(f)$ estimated from the full spectrum or the linear spectrum only, using Eq. (5) for both cases. The value of I is found to increase sharply from less than 0.01 at $f = 2f_p$, to 0.11 at $f = 4f_p$, and possibly up to 0.2 at $f = 5f_p$, not too far from the 0.5π value proposed in previous studies, but our data are less reliable above $4.25f_p$.

However, this estimation is very naive because the interaction that produces acoustic waves is between wave components \mathbf{k}_1 and \mathbf{k}_2 that give $\mathbf{K} = \mathbf{k}_1 + \mathbf{k}_2 \simeq 0$. This interaction can involve both linear components and nonlinear components but not the interaction of a linear component with a nonlinear component of the same frequency because that will not give a near-zero wavenumber. Our observations suggest that at frequencies above $3f_p$, the acoustic generation theory should be revised to properly separate linear and nonlinear modes. That effort is beyond the scope of the present paper.

6. Conclusions

Using a stereo video acquisition system, we have revealed new features of the wave spectrum at intermediate scales between the dominant waves and the

short gravity waves that can be relevant for the interpretation of remote sensing data, air–sea fluxes, and underwater acoustics. Our measurements give detailed spectral measurements of young waves that extend the known bimodal distribution (e.g., Long and Resio 2007; Romero and Melville 2010) to higher frequencies, up to 4.25 times the peak frequency, where the angular separation of the two peaks of the directional distribution is as large as 150° . The use of space–time analysis removes the 180° ambiguity in wave propagation direction that was present in previous studies. This unambiguous spectrum allows an estimation of the so-called overlap integral to which the source of acoustic and seismic waves is proportional (Hasselmann 1963; Ardhuin and Herbers 2013). It also allows a separation of some nonlinear contributions to the wave spectrum from the linear free wave part of the spectrum. That analysis reveals that the Doppler shifting of short waves by long waves has a negligible effect on the frequency spectrum up to $5f_p$, while the nonlinearity of the waves, well predicted by Janssen (2009)’s application of the Krasitskii (1994) canonical transform, is an important source of deviation from linear wave theory. In addition to the data record analyzed here, the three other records discussed in Leckler (2013) give similar results but correspond to wind speed and wave ages that only vary by 10%. More data will be needed to generalize these findings to more mature seas. The data described here already provide useful constraints for concepts and parameterizations of the wind-wave energy balance and the interpretation of underwater acoustic data, such as presented by Farrell and Munk (2010).

Acknowledgments. F. A. and F. L. were supported by a FP7-ERC Grant Number 240009 for the IOWAGA project; the U.S. National Ocean Partnership Program, under Grant N00014-10-1-0383; and Labex Mer under Grant ANR-10-LABX-19-01, with a preliminary experiment supported by CNES as part of the CFOSAT preparation program. V. D. was supported by the Ministry of Education and Science of the Russian Federation under the Federal Target Program “Research and development on priority directions of scientific and technological complex of Russia for 2014–2020” (unique project identifier RFMEFI57714 \times 0110) and by Russian Fund of Fundamental Researches (Grant 13-05-90429). We thank all the staff of the Marine Hydrophysics Institute, especially Vladimir Smolov, Yuri Yurovski, and Maria Yurovsakaya for making the experiment possible and discussions on stereo reconstructions that led to improvements of our early processing methods. Thanks also go to Peter Janssen for providing his canonical transform code, which is now

included in the ECMWF WAM and WAVEWATCH III models. Comments from two anonymous reviewers helped clarify the paper.

REFERENCES

- Andrews, D. G., and M. E. McIntyre, 1978: On wave-action and its relatives. *J. Fluid Mech.*, **89**, 647–664, doi:10.1017/S0022112078002785; Corrigendum, **95**, 796, doi:10.1017/S0022112079001737.
- Ardhuin, F., and T. H. C. Herbers, 2013: Noise generation in the solid earth, oceans and atmosphere, from nonlinear interacting surface gravity waves in finite depth. *J. Fluid Mech.*, **716**, 316–348, doi:10.1017/jfm.2012.548.
- , L. Marié, N. Rasche, P. Forget, and A. Roland, 2009: Observation and estimation of Lagrangian, Stokes, and Eulerian currents induced by wind and waves at the sea surface. *J. Phys. Oceanogr.*, **39**, 2820–2838, doi:10.1175/2009JPO4169.1.
- , and Coauthors, 2013: A numerical model for ocean ultra-low frequency noise: Wave-generated acoustic-gravity and Rayleigh modes. *J. Acoust. Soc. Amer.*, **134**, 3242–3259, doi:10.1121/1.4818840.
- Banner, M. L., 1990: Equilibrium spectra of wind waves. *J. Phys. Oceanogr.*, **20**, 966–984, doi:10.1175/1520-0485(1990)020<0966:ESOWW>2.0.CO;2.
- , and O. M. Phillips, 1974: On the incipient breaking of small scale waves. *J. Fluid Mech.*, **65**, 647–656, doi:10.1017/S0022112074001583.
- , I. S. F. Jones, and J. C. Trinder, 1989: Wavenumber spectra of short gravity waves. *J. Fluid Mech.*, **198**, 321–344, doi:10.1017/S0022112089000157.
- Benetazzo, A., 2006: Measurements of short water waves using stereo matched image sequences. *Coastal Eng.*, **53**, 1013–1032, doi:10.1016/j.coastaleng.2006.06.012.
- , F. Fedele, G. Gallego, P.-C. Shih, and A. Yezzi, 2012: Off-shore stereo measurements of gravity waves. *Coastal Eng.*, **64**, 127–138, doi:10.1016/j.coastaleng.2012.01.007.
- , F. Bergamasco, F. Barbariol, A. Torsello, S. Carniel, and M. Scavo, 2014: Towards an operational stereo system for directional wave measurements from moving platforms. *Proc. 33rd Int. Conf. on Ocean, Offshore and Arctic Engineering, OMAE 2014*, San Francisco, CA, ASME, OMAE2014-24024, doi:10.1115/OMAE2014-24024.
- Benoit, M., P. Frigaard, and H. A. Schäffer, 1997: Analyzing multidirectional wave spectra: A tentative classification of available methods. *Proc. 27th IAHR World Conf.*, San Francisco, CA, IAHR, 131–158.
- Broche, P., J. C. de Maistre, and P. Forget, 1983: Mesure par radar décimétrique cohérent des courants superficiels engendrés par le vent. *Oceanol. Acta*, **6**, 43–53.
- Chase, J. L., and Coauthors, 1957: *The Directional Spectrum of a Wind Generated Sea as Determined from Data Obtained by the Stereo Wave Observation Project*. New York University, College of Engineering, Research Division, Department of Meteorology and Oceanography and Engineering Statistics Group, 292 pp.
- Creamer, D. B., F. Henyey, R. Schult, and J. Wright, 1989: Improved linear representation of ocean surface waves. *J. Fluid Mech.*, **205**, 135–161, doi:10.1017/S0022112089001977.
- Duenneber, F. K., R. Lukas, E.-M. Nosal, J. Aucan, and R. A. Weller, 2012: Wind, waves, and acoustic background levels at station ALOHA. *J. Geophys. Res.*, **117**, C03017, doi:10.1029/2011JC007267.
- Dugan, J. P., and Coauthors, 2001a: Airborne optical system for remote sensing of ocean waves. *J. Atmos. Oceanic Technol.*, **18**, 1267–1275, doi:10.1175/1520-0426(2001)018<1267:AOSFRS>2.0.CO;2.
- , C. C. Piotrowsky, and J. Z. Williams, 2001b: Water depth and surface current retrievals from airborne optical measurements of surface gravity wave dispersion. *J. Geophys. Res.*, **106**, 16 903–16 915, doi:10.1029/2000JC000369.
- Elfouhaily, T., B. Chapron, K. Katsaros, and D. Vandemark, 1997: A unified directional spectrum for long and short wind-driven waves. *J. Geophys. Res.*, **102**, 15 781–15 796, doi:10.1029/97JC00467.
- Evans, K. C., 1998: Observations of the directional spectrum of fetch-limited waves. *J. Phys. Oceanogr.*, **28**, 495–512, doi:10.1175/1520-0485(1998)028<0495:OOTDSO>2.0.CO;2.
- Farrell, W. E., and W. Munk, 2008: What do deep sea pressure fluctuations tell about short surface waves? *Geophys. Res. Lett.*, **35**, L19605, doi:10.1029/2008GL035008.
- , and —, 2010: Booms and busts in the deep. *J. Phys. Oceanogr.*, **40**, 2159–2169, doi:10.1175/2010JPO4440.1.
- Fedele, F., 2012: Space-time extremes in short-crested storm seas. *J. Phys. Oceanogr.*, **42**, 1601–1615, doi:10.1175/JPO-D-11-0179.1.
- , A. Benetazzo, and G. F. Forristall, 2011: Space-time waves and spectra in the northern Adriatic sea via a wave acquisition stereo system. *Proc. 30th Int. Conf. on Ocean, Offshore and Arctic Engineering, OMAE 2011*, Rotterdam, Netherlands, ASME, OMAE2011-49924, doi:10.1115/OMAE2011-49924.
- , —, G. Gallego, P.-C. Shih, A. Yezzi, F. Barbariol, and F. Ardhuin, 2013: Space-time measurements of oceanic sea states. *Ocean Modell.*, **70**, 103–115, doi:10.1016/j.ocemod.2013.01.001.
- Forristall, G. Z., 1981: Measurements of a saturation range in ocean wave spectra. *J. Geophys. Res.*, **86**, 8075–8084, doi:10.1029/JC086iC09p08075.
- Gallego, G., A. Benetazzo, A. Yezzi, and F. Fedele, 2008: Wave statistics and spectra via a variational wave acquisition stereo system. *Proc. 27th Int. Conf. on Offshore Mechanics and Arctic Engineering, OMAE 2008*, Estoril, Portugal, ASME, OMAE2008-57160, doi:10.1115/OMAE2008-57160.
- , A. Yezzi, F. Fedele, and A. Benetazzo, 2011: A variational stereo method for the three-dimensional reconstruction of ocean waves. *IEEE Trans. Geosci. Remote Sens.*, **49**, 4445–4457, doi:10.1109/TGRS.2011.2150230.
- Garrett, C., and J. Smith, 1976: On the interaction between long and short surface waves. *J. Phys. Oceanogr.*, **6**, 925–930, doi:10.1175/1520-0485(1976)006<0925:OTIBLA>2.0.CO;2.
- Hartley, R., and A. Zisserman, 2003: *Multiple View Geometry in Computer Vision*. 2nd ed. Cambridge University Press, 655 pp.
- Hasselmann, K., 1962: On the non-linear energy transfer in a gravity wave spectrum Part 1. General theory. *J. Fluid Mech.*, **12**, 481–501, doi:10.1017/S0022112062000373.
- , 1963: A statistical analysis of the generation of microseisms. *Rev. Geophys.*, **1**, 177–210, doi:10.1029/RG001i002p00177.
- , and Coauthors, 1973: Measurements of wind-wave growth and swell decay during the Joint North Sea Wave Project. *Deut. Hydrogr. Z.*, **8**, 1–95.
- Holthuijsen, L. H., 1983: Observations of the directional distribution of ocean wave energy. *J. Phys. Oceanogr.*, **13**, 191–207, doi:10.1175/1520-0485(1983)013<0191:OOTDDO>2.0.CO;2.
- Hwang, P. A., D. W. Wang, E. J. Walsh, W. B. Krabill, and R. N. Swift, 2000: Airborne measurement of the wavenumber spectra of ocean surface waves. Part I: Spectral slope and dimensionless

- spectral coefficient. *J. Phys. Oceanogr.*, **30**, 2753–2767, doi:10.1175/1520-0485(2001)031<2753:AMOTWS>2.0.CO;2.
- Janssen, P. A. E. M., 2009: On some consequences of the canonical transformation in the Hamiltonian theory of water waves. *J. Fluid Mech.*, **637**, 1–44, doi:10.1017/S0022112009008131.
- Kirby, J. T., and T.-M. Chen, 1989: Surface waves on vertically sheared flows: Approximate dispersion relations. *J. Geophys. Res.*, **94**, 1013–1027, doi:10.1029/JC094iC01p01013.
- Kosnik, M. V., and V. A. Dulov, 2011: Extraction of short wind wave spectra from stereo images of the sea surface. *Meas. Sci. Technol.*, **22**, 015504, doi:10.1088/0957-0233/22/1/015504.
- Krasitskii, V. P., 1994: On reduced equations in the Hamiltonian theory of weakly nonlinear surface waves. *J. Fluid Mech.*, **272**, 1–20, doi:10.1017/S0022112094004350.
- Krogstad, H. E., 2005: Conventional analysis of wave measurement arrays. *Measuring and Analysing the Directional Spectra of Ocean Waves*, D. Hauser et al., Eds., Office for Official Publications of the European Communities, 56–71.
- , and K. Trulsen, 2010: Interpretations and observations of ocean wave spectra. *Ocean Dyn.*, **60**, 973–991, doi:10.1007/s10236-010-0293-3.
- Kudryavtsev, V., D. Akimov, J. Johannessen, and B. Chapron, 2005: On radar imaging of current features: 1. Model and comparison with observations. *J. Geophys. Res.*, **110**, C07016, doi:10.1029/2004JC002505.
- Leckler, F., 2013: Observation et modélisation du déferlement des vagues. Ph.D. thesis, Ecole doctorale des Sciences de la Mer, Université Européenne de Bretagne, 240 pp. [Available online at <http://tinyurl.com/leckler-thesis>.]
- Long, C. E., and D. T. Resio, 2007: Wind wave spectral observations in Currituck Sound, North Carolina. *J. Geophys. Res.*, **112**, C05001, doi:10.1029/2006JC003835.
- Longuet-Higgins, M. S., 1950: A theory of the origin of microseisms. *Philos. Trans. Roy. Soc. London*, **A243**, 1–35, doi:10.1098/rsta.1950.0012.
- , D. E. Cartwright, and N. D. Smith, 1963: Observations of the directional spectrum of sea waves using the motions of a floating buoy. *Ocean Wave Spectrum*, Prentice-Hall, 111–136.
- Lygre, A., and H. E. Krogstad, 1986: Maximum entropy estimation of the directional distribution in ocean wave spectra. *J. Phys. Oceanogr.*, **16**, 2052–2060, doi:10.1175/1520-0485(1986)016<2052:MEEOTD>2.0.CO;2.
- Plant, W. J., and G. Farquharson, 2012: Origins of features in wave number-frequency spectra of space-time images of the ocean. *J. Geophys. Res.*, **117**, C06015, doi:10.1029/2012JC007986.
- Quilfen, Y., B. Chapron, A. Bentamy, J. Gourrion, T. Elfouhaily, and D. Vandemark, 1999: Global ERS 1 and 2 and NSCAT observations: Upwind/crosswind and upwind/downwind measurements. *J. Geophys. Res.*, **104**, 11 459–11 469, doi:10.1029/1998JC900113.
- Raschle, N., and F. Ardhuin, 2009: Drift and mixing under the ocean surface revisited: Stratified conditions and model-data comparisons. *J. Geophys. Res.*, **114**, C02016, doi:10.1029/2007JC004466.
- Romero, L., and K. W. Melville, 2010: Airborne observations of fetch-limited waves in the Gulf of Tehuantepec. *J. Phys. Oceanogr.*, **40**, 441–465, doi:10.1175/2009JPO4127.1.
- Schumacher, A., 1939: Stereophotogrammetrische Wellenaufnahmen. Wissenschaftliche Ergebnisse der deutschen atlantischen Expedition auf dem Forschungs- und Vermessungsschiff “Meteor” 1925-1927 Tech. Rep., 86 pp.
- Stewart, R. H., and J. W. Joy, 1974: HF radio measurements of surface currents. *Deep-Sea Res. Oceanogr. Abstr.*, **21**, 1039–1049, doi:10.1016/0011-7471(74)90066-7.
- Stokes, G. G., 1880: On the theory of oscillatory waves. *Mathematical and Physical Papers*, Vol. 1, 197–229, doi:10.1017/CBO9780511702242.013.
- Sutherland, P., and W. K. Melville, 2013: Field measurements and scaling of ocean surface wave-breaking statistics. *Geophys. Res. Lett.*, **40**, 3074–3079, doi:10.1002/grl.50584.
- Taklo, T. M. A., K. Trulsen, O. Gramstad, H. E. Krogstad, and A. Jensen, 2015: Measurement of the dispersion relation for random surface gravity waves. *J. Fluid Mech.*, **766**, 326–336, doi:10.1017/jfm.2015.25.
- Tayfun, M. A., 1980: Narrow-band nonlinear sea waves. *J. Geophys. Res.*, **85**, 1548–1552, doi:10.1029/JC085iC03p01548.
- Weber, B. L., and D. E. Barrick, 1977: On the nonlinear theory for gravity waves on the ocean’s surface. Part I: Derivations. *J. Phys. Oceanogr.*, **7**, 3–10, doi:10.1175/1520-0485(1977)007<0003:OTNTEFG>2.0.CO;2.
- Young, I. R., 2010: The form of the asymptotic depth-limited wind-wave spectrum: Part III—Directional spreading. *Coastal Eng.*, **57**, 30–40, doi:10.1016/j.coastaleng.2009.09.001.
- Yueh, S. H., W. Tang, A. G. Fore, G. Neumann, A. Hayashi, A. Freedman, J. Chaubell, and G. S. E. Lagerloef, 2013: L-band passive and active microwave geophysical model functions of ocean surface winds and applications to *Aquarius* retrieval. *IEEE Trans. Geosci. Remote Sens.*, **51**, 4619–4632, doi:10.1109/TGRS.2013.2266915.
- Yurovskaya, M. V., V. A. Dulov, B. Chapron, and V. N. Kudryavtsev, 2013: Directional short wind wave spectra derived from the sea surface photography. *J. Geophys. Res. Oceans*, **118**, C12024, doi:10.1002/jgrc.20296.
- Zappa, C. J., M. L. Banner, H. Schultz, J. R. Gemmrich, R. P. Morison, D. A. LeBel, and T. Dickey, 2012: An overview of sea state conditions and air-sea fluxes during RaDyO. *J. Geophys. Res.*, **117**, C00H19, doi:10.1029/2011JC007336.